Aalborg Universitet

Transient Stability of Voltage-Source Converters With Grid-Forming Control

A Design-Oriented Study

Pan, Donghua; Wang, Xiongfei; Liu, Fangcheng; Shi, Rongliang

Transient Stability of Voltage-Source Converters with Grid-Forming Control: A Design-Oriented Study

Donghua Pan, *Member, IEEE*, Xiongfei Wang, *Senior Member, IEEE*, Fangcheng Liu, and Rongliang Shi

Abstract—**Driven by the large-scale integration of distributed power resources, grid-connected voltage-source converters (VSCs) are increasingly required to operate as grid-forming units to regulate the system voltage/frequency and emulate the inertia. While various grid-forming control schemes have been reported, their transient behaviors under large-signal disturbances are still not fully explored. This paper addresses this issue by presenting a design-oriented transient stability analysis of the grid-forming VSCs. First, four typical grid-forming control schemes, namely the power-synchronization control (PSC), the basic droop control, the droop control with low-pass filters (LPFs), and the virtual synchronous generator (VSG) control, are systematically reviewed, whose dynamics are characterized by a general large-signal model. Based on this model, a comparative analysis on the transient stabilities of different control schemes is then carried out. It reveals that the PSC and the basic droop control can retain a stable operation as long as there are equilibrium points, due to their non-inertial transient responses; while the droop control with LPFs and the VSG control can be destabilized even if the equilibrium points exist, due to the lack of damping on their inertial transient responses. With the phase portrait, the underlying stability mechanism is explicitly elaborated, and the quantitative impacts of the controller gains and the virtual inertia are clearly identified. Subsequently, controller design guidelines are proposed to enhance the system damping as well as the transient stability. Finally, experimental results are provided to verify the theoretical analysis.**

Index Terms—**Grid-forming control, large-signal disturbance, transient stability, virtual inertia, voltage-source converters.**

I. INTRODUCTION

With the increasing integration of renewable energy resources, the legacy power grids dominated by centralized synchronous generators (SGs) are evolving into distributed power generation systems (DPGSs), which are interfaced by voltage-source converters (VSCs) [1]. The full controllability of VSCs enables a flexible operation of DPGSs, but it poses also new challenges. Currently, the majority of VSCs are controlled as current sources, which follow the voltage and the frequency predefined by the existing SGs [2], [3]. This current regulation strategy is called the *grid-following* control, whose stable operation relies on a

stiff grid condition [4], [5]. However, as the penetration of DPGSs goes high, the stiffness of the power grid is reduced. To secure a reliable electric power supply, VSCs are required to participate in forming the system voltage and frequency, which is realized by the *grid-forming* control. Different from grid-following converters, grid-forming units behave as voltage sources, which possess a number of superior features, such as the black-start capability, the enhanced synchronization performance in weak grids, and the rate of change of frequency (RoCoF) support [6], [7].

To implement the grid-forming control, an intuitive solution is to operate VSCs in a similar way as SGs. Various control schemes have thus been proposed, of which the simplest one is the *P-f* and *Q-V* droop method [8], [9]. The droop control mimics the behavior of SGs on frequency and voltage regulations, which reduce the frequency when the active power increases and reduce the voltage amplitude when the reactive power increases. This principle has been used in the power-synchronization control (PSC) for VSCs connected to the weak grid [10], [11]. However, there is a lack of synthetic inertia with the droop control, which can lead to a large frequency deviation and a high RoCoF when operating with existing SGs [12], [13]. To address this issue, the concept of a virtual synchronous generator (VSG) is proposed by introducing an inertia emulating term into the basic droop control [14]–[17]. It has been shown that such a virtual inertia can be realized by a low-pass filter (LPF) added in the power control loop [18], [19].

While benefiting from the SG-like operation, grid-forming VSCs also suffer from stability problems under grid disturbances. Substantial research efforts have been devoted to this issue, with the main focus on small-signal disturbances [8]–[11], [20], [21]. The small-signal stability is assessed by linearizing VSCs around an equilibrium operating point, thus it is not applicable if the operating point is changed by large-signal disturbances, e.g., a fault on transmission lines, a severe grid voltage sag, and a large load swing. Under such circumstances, the *transient stability* of VSCs, which characterizes the ability of VSCs to maintain synchronization with the grid [22], is concerned, and it attracts increasing research interests recently. In [23] and [24], a transient instability phenomenon of a basic droop-controlled VSC was found in the case of a current saturation due to the grid voltage sag. In [25], a VSC with the PSC was studied, and its transient behaviors were analyzed under different types of grid faults. In [26], the droop control with an LPF (the inertial term) was focused, and its transient stability was evaluated with the Lyapunov function. In those works, the transient
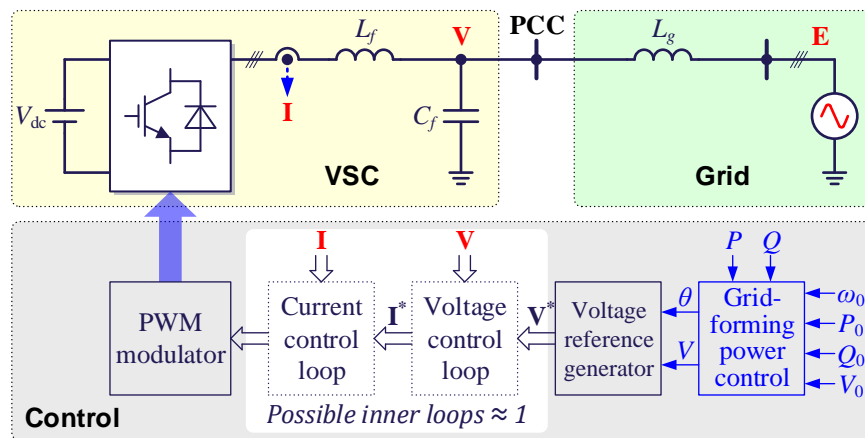
Fig. 1. Single-line diagram of a three-phase VSC with the grid-forming control.

stability is believed to be merely determined by the active power control, whereas the effect of the reactive power control is overlooked. This can lead to an inaccurate stability prediction, due to the cross coupling between the two control loops. A qualitative analysis of the reactive power control was illustrated in [27] by means of the power-angle (P-δ) curve, which shows its deteriorative effect on the transient stability of the VSG. Although intuitive, it lacks an accurate identification of how and to what extent the transient behavior is affected by the reactive power control as well as other control items, including the droop gains and the virtual inertia (or the LPFs). This is actually a fundamental challenge in the transient stability analysis, due to the high complexity inherent in the large-signal nonlinear dynamic responses.

This paper addresses this challenge by presenting a design-oriented transient stability analysis of grid-forming VSCs, which quantifies the impacts of the reactive power control, the droop gains, and the inertia emulating LPFs. To begin with, four typical grid-forming control schemes, namely the PSC, the basic droop control, the droop control with LPFs, and the VSG control, are systematically reviewed in Section II. These control schemes are further classified into the non-inertial grid-forming control and the inertial grid-forming control. A general large-signal model, which accounts for the cross coupling between the active and the reactive power loops, is then introduced. Based on this model, transient stabilities of different control schemes are comparatively studied in Sections III and IV. It is shown that the PSC and the basic droop control can retain a stable operation as long as there are equilibrium points, due to their non-inertial transient responses; while the droop control with LPFs and the VSG control can be destabilized even if the equilibrium points exist, due to the lack of damping on their inertial transient responses. The instability mechanism is explicitly revealed by means of the phase portrait, and design rules for both the droop gains and the inertia emulating LPFs are proposed to enhance the system damping as well as the transient stability. Moreover, the stability challenge in the high-inertia grid-forming VSC is addressed by optimizing the controller parameters, and the influence of the virtual impedance control on the transient behavior is discussed. Finally, the theoretical

predictions are confirmed by experimental results in Section V, before drawing the conclusion in Section VI.

II. LARGE-SIGNAL MODELING OF GRID-FORMING VSCS

Fig. 1 shows the single-line diagram of a three-phase pulse-width modulation (PWM) VSC connecting to the grid. Inductor L_f and capacitor C_f form an output LC filter of the VSC. The grid impedance at the point of common coupling (PCC) is considered as a pure inductance L_g. The grid voltage is represented by a vector $\mathbf{E}$, which has an amplitude E and a frequency ω_0.

Generally, in the grid-following operation, the VSC controls the dc voltage to balance the power supplied by renewable sources, such as the maximum power tracked by the wind turbine or the photovoltaic stack [28], [29]. However, in the grid-forming operation, the VSC is required to provide the power demanded by the grid in order to support the system voltage and frequency. For this purpose, the dc voltage control is usually taken over by another component, which can be either a front-end converter (e.g., high-voltage dc system [10], [11]) or an energy storage unit [16], [17] connected to the dc-link. Thus, a constant dc voltage V_{dc} can be assumed in studying the grid-forming VSC.

As shown in Fig. 1, the VSC is regulated by a grid-forming power control loop to yield the phase and the voltage amplitude commands, i.e., θ and V, which are then combined to generate the voltage reference vector $\mathbf{V}^*$. In some grid-forming VSCs, such as the synchronverter [16], [17] and the universal controller proposed in [30] and [31], $\mathbf{V}^*$ is directly fed to the PWM modulator to implement this voltage at the output of the VSC. This control strategy is simple, but it lacks capabilities on the voltage regulation and the current limitation, due to its open-loop nature on the voltage and current control. An alternative solution is to employ an inner voltage loop, which regulates the VSC output voltage $\mathbf{V}$ to track the reference $\mathbf{V}^*$. A current loop is cascaded to the voltage loop to actively damp the LC resonance and thus enhance the system stability [8], [20]. Moreover, a current limitation scheme is also embedded by limiting the current reference amplitude $|\mathbf{I}^*|$ to prevent the VSC from the overcurrent blocking [10], [11].
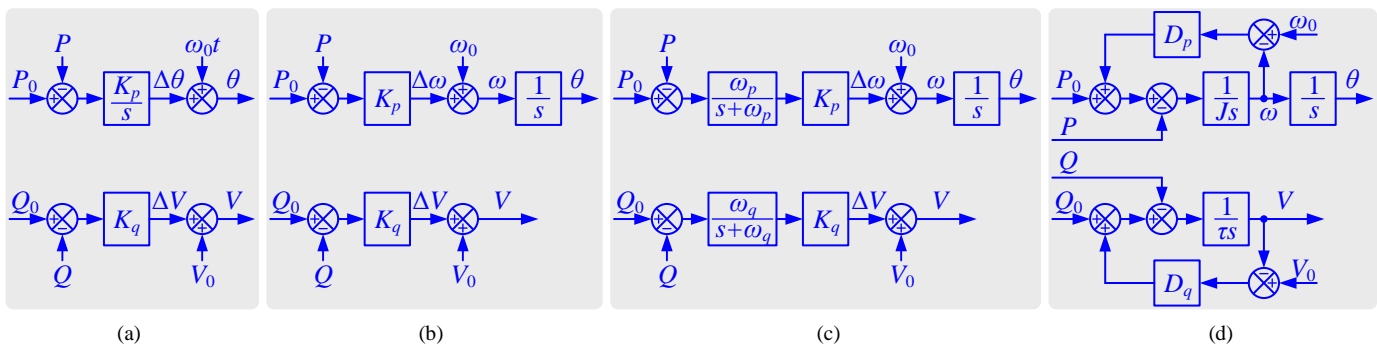
Fig. 2. Four typical grid-forming control schemes. (a) PSC. (b) Basic droop control. (c) Droop control with LPFs. (d) VSG control.

Despite the different control architectures, their transient responses are quite similar, due to the decoupled timescales between the outer loop and the inner loop. In general, the dynamic of the outer power loop is over ten times slower than that of the inner voltage and current loop [32]. Hence, when analyzing the transient stability issue caused by the power loop, the inner dual-loop voltage control can be regarded as a unity gain with an ideal reference tracking [23]–[26], i.e., $\mathbf{V} = \mathbf{V}^*$ and $|\mathbf{V}| = V$, which is exactly the same as that without an inner loop. Thus, for both control architectures, the following analysis is applicable.

Fig. 2 shows four typical grid-forming control schemes, where the PSC is illustrated first. The PSC was proposed in [10], which aims at synchronizing the VSC with the grid through a power-synchronization loop, i.e., the active power loop. Fig. 2(a) shows its control diagram. The active power error is integrated to a phase increment $\Delta\theta$, which is added to the static phase $\omega_0 t$, yields θ. Considering $\theta = \omega t$, with ω being the frequency of the VSC, the control law can be written as

$$\theta = \omega t = \omega_0 t + K_p \int (P_0 - P) \;\Rightarrow\; \omega = \omega_0 + K_p (P_0 - P) \tag{1}$$

where P and P_0 are the active power and its reference, respectively, and K_p is the controller gain.

The reactive power control is flexible, yet not focused in [10]. Here, the reactive power error is processed by a proportional controller K_q to generate the voltage increment ΔV, which is added to the voltage reference V_0, yields V, i.e.,

$$V = V_0 + K_q (Q_0 - Q) \tag{2}$$

where Q and Q_0 are the reactive power and its reference, respectively.

From (1) and (2), it is clear to see that the control law of the PSC is the same as that of the basic droop control. Such an equivalence can also be identified through transformations of the control diagram. First, the static phase $\omega_0 t$ can be seen as an integration of ω_0. Then, combining this integrator with the integrator of the controller K_p/s, an equivalent block diagram is obtained, as shown in Fig. 2(b), which exactly depicts the mechanism of the basic droop control [8], [9].

To remove the fluctuations in measured power components caused by the load unbalance, LPFs are usually added into power control loops [20], [26], as shown in Fig. 2(c). For the generality, two LPFs with different cutoff frequencies, i.e., ω_p and ω_q, are employed in the active and the reactive power loops. Consequently, control laws can be written as

$$\omega = \omega_0 + K_p \cdot \frac{\omega_p}{s + \omega_p} \cdot (P_0 - P) \tag{3}$$

$$V = V_0 + K_q \cdot \frac{\omega_q}{s + \omega_q} \cdot (Q_0 - Q). \tag{4}$$

Although unintentionally, the use of LPFs introduces a virtual inertia to the VSC, similar to that in the VSG [18]. To figure out this effect, the VSG control is revisited here, as shown in Fig. 2(d). In the VSG, the P-f droop is implemented by adjusting the active power reference according to the frequency difference $\omega_0 - \omega$, with D_p being the droop gain (also known as the damping factor [19]). Unlike the PSC and the basic droop control, the active power error is not used to regulate the phase, but the frequency in order to synthesize the inertia J and emulate the swing equation, which are basic properties of the SG. Similarly, the Q-V droop is implemented by adjusting the reactive power reference according to the voltage difference $V_0 - V$, with D_q being the droop gain. Then, the reactive power error is processed by an integrator $1/(\tau s)$ to obtain V. Thus, we can get

$$\omega = \frac{1}{Js}\left[D_p (\omega_0 - \omega) + P_0 - P \right]$$
$$\Rightarrow\; \omega = \frac{D_p}{Js + D_p} \cdot \omega_0 + \frac{1}{Js + D_p} \cdot (P_0 - P) \tag{5}$$

$$V = \frac{1}{\tau s}\left[D_q (V_0 - V) + Q_0 - Q \right]$$
$$\Rightarrow\; V = \frac{D_q}{\tau s + D_q} \cdot V_0 + \frac{1}{\tau s + D_q} \cdot (Q_0 - Q). \tag{6}$$

Note that (5) and (6) have been simplified by ignoring the low-pass filtering of constant terms ω_0 and V_0. It is worth mentioning that the measured VSC output voltage amplitude V_m can be fed back to implement the Q-V droop, instead of the calculated command V [16], [17], [21]. In fact, this will not make much difference on the transient response, since V_m can
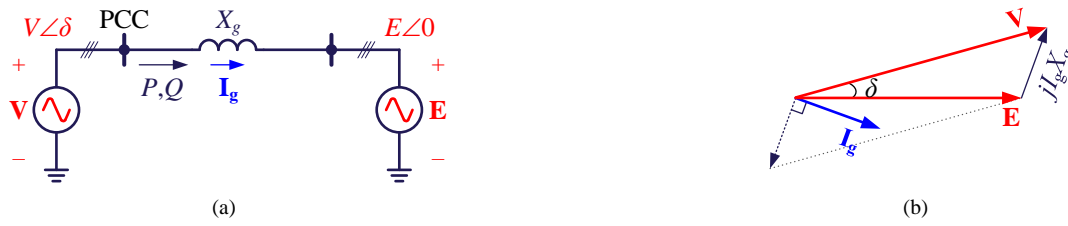
Fig. 3. (a) Simplified circuit and (b) phasor diagram of the grid-forming VSC.

well track V as discussed above and it can be replaced with V in the theoretical analysis. Observing (3) – (6), it can be found that the droop control with LPFs is the same as the VSG control. The equivalence between them is expressed as

$$J = \frac{1}{K_p \omega_p}, \ D_p = \frac{1}{K_p}, \ \tau = \frac{1}{K_q \omega_q}, \ D_q = \frac{1}{K_q}. \quad (7)$$

Due to the equivalences discussed above, the four grid-forming control schemes can be categorized into two types: one is the non-inertial grid-forming control, including the PSC and the basic droop control, which is a *first-order* system, and the other is the inertial grid-forming control, including the droop control with LPFs and the VSG control, which is a *second-order* system. Moreover, the non-inertial grid-forming control can be seen as a special case of the inertial one, where $\omega_p = \omega_q = \infty$ or $J = \tau = 0$. Hence, they can be represented by one general model. Here, we select the droop control with LPFs as the representative.

It is worth noting that various grid-forming control schemes can be constructed based on the aforementioned four typical ones. For example, an evolving VSG control was proposed in [33] by replacing the damping factor D_p with a high-pass filter (a damping function). Moreover, there are other possibilities for the damping function, which were thoroughly reviewed in [34] and [35]. A modification on the damping mechanism will alter the swing equation, leading to a higher-order dynamic response [36]. However, the motivation of this paper is not to cover all the control possibilities, but to establish an analytical method for the transient stability of grid-forming VSCs by focusing on the basic control schemes. The developed methodology provides a theoretical basis for more sophisticated grid-forming operations, on which further studies can be easily drawn to characterize the higher-order dynamics.

Recalling Fig. 1, a simplified circuit of the grid-forming VSC is given in Fig. 3(a), where $X_g = \omega_0 L_g$ is the grid impedance. Taking the voltage vector $\mathbf{E}$ as a reference, and assuming the phase difference between $\mathbf{V}$ and $\mathbf{E}$ is δ, i.e., the power angle, we can obtain $\mathbf{E} = E \angle 0$, $\mathbf{V} = V \angle \delta$, whose phasor diagram is shown in Fig. 3(b). From which, P and Q from the PCC can be derived as

$$P = \frac{3}{2} \cdot \frac{EV \sin \delta}{X_g} \quad (8)$$

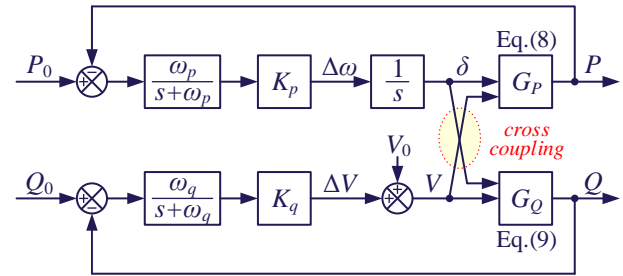$$Q = \frac{3}{2} \cdot \frac{V^2 - EV \cos \delta}{X_g}. \quad (9)$$

Fig. 4. Large-signal model of the grid-forming VSC.

Obviously, both P and Q are related to δ and V, which means the active power loop that commands δ and the reactive power loop that commands V are coupled with each other. Considering this cross coupling, a large-signal model of the power control loops is obtained, as shown in Fig. 4, where G_P and G_Q are expressions of P and Q, i.e., (8) and (9), respectively. Based on this model, the transient stability of grid-forming VSCs will be elaborated in the following sections.

III. TRANSIENT STABILITY OF NON-INERTIAL GRID-FORMING CONTROL — PSC AND BASIC DROOP CONTROL

Generally, the transient stability of the VSC is dependent on the dynamic response of δ under a large disturbance (usually a grid fault). The VSC will be stable if δ can return to its original value or reach another steady-state value, and will be unstable if δ diverges to infinite. The grid faults can happen in various types, where a large fault current may be accompanied [37], [38]. If the overcurrent limit of the VSC is triggered by the fault, the grid-forming control will be switched to the vector current control (a grid-following operation) [10], [11], [25], in which the VSC output current $\mathbf{I}$ is regulated to track the limited reference $\mathbf{I}^*$ to avoid an overcurrent. The grid synchronization in this scenario is realized by the phase-locked loop (PLL), which determines the transient behavior of the VSC. The impact of the PLL on the transient stability of grid-following VSCs has been extensively discussed in [39]–[42], which is another topic and beyond the scope of our work. Therefore, in order to reveal the VSC's transient response characterized by the grid-forming control, the grid fault that do not trigger the overcurrent limit is focused.

To establish the basic concept of the transient stability, the non-inertial grid-forming control schemes, i.e., the PSC and the basic droop control, are discussed first. Recalling (8) and Fig. 4, letting $\omega_p = \omega_q = \infty$, the derivative of δ, i.e., $\Delta\omega$, is obtained as
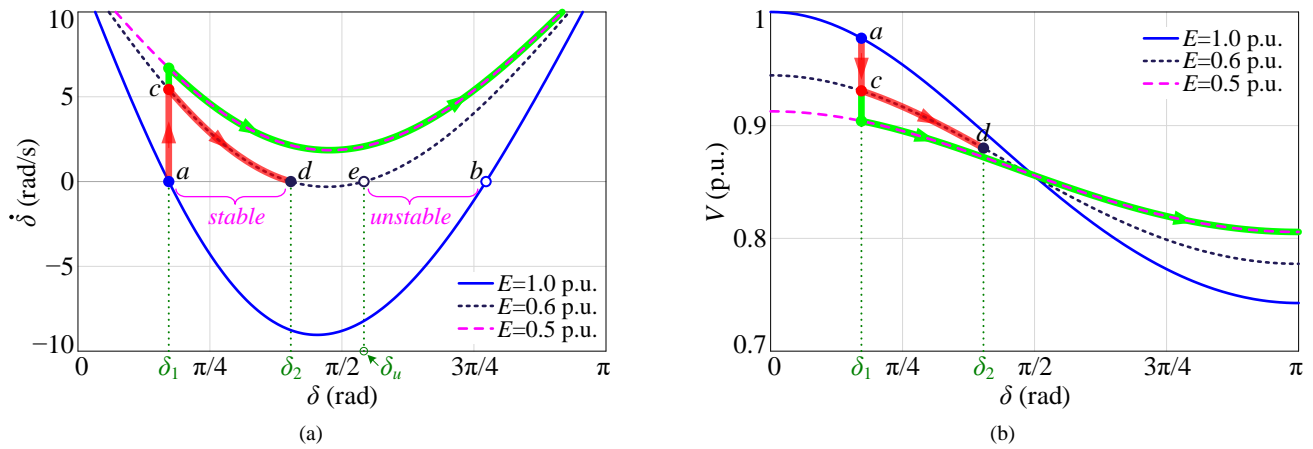
Fig. 5. (a) Phase portraits and (b) V-δ curves of the non-inertial grid-forming control ($\omega_p = \omega_q = \infty$).

$$\dot{\delta} = K_p \left(P_0 - P \right) = K_p \left(P_0 - \frac{3}{2} \cdot \frac{EV \sin \delta}{X_g} \right). \tag{10}$$

In the steady-state, the VSC operates at the grid frequency ω_0, thus $\Delta\omega = \dot{\delta} = 0$ and $P = P_0$ (the equilibrium point). However, the dynamic response of δ is implicit in (10), since it is coupled with the other controlled variable V, which is commanded by the reactive power loop. To quantify this coupling effect, we first rewrite the Q-V droop law by substituting (9) into (2), i.e.,

$$V = V_0 + K_q \left(Q_0 - \frac{3}{2} \cdot \frac{V^2 - EV \cos \delta}{X_g} \right) \tag{11}$$

which is obviously a quadratic equation of V. Solving this equation, V is found related to δ by (12). Substituting (12) into (10), the dynamic equation of δ, considering the effect of reactive power control, can be obtained as (13), shown at the bottom of this page.

Hence, the mathematical relationship between $\dot{\delta}$ and δ is explicitly derived by (13), which is critical for the transient stability analysis. However, due to the high nonlinearity, it is difficult to acquire an analytical solution of (13). In contrast, a graphical evaluation of (13) can be easily carried out by the $\dot{\delta}$-δ curve, which is the so-called phase portrait [43]. Based on the phase portrait, the change of δ can be readily predicted, i.e., δ will increase if $\dot{\delta} > 0$ and decrease if $\dot{\delta} < 0$,

and $\dot{\delta} = 0$ corresponds to the equilibrium points. The existing of equilibrium points means that the maximum power that can be transferred between $\mathbf{V}$ and $\mathbf{E}$ is larger than the commanded power P_0. According to the parameters listed in Table I, the phase portrait under a normal condition ($E = 1$ p.u.) is plotted with the solid line in Fig. 5(a). There are two equilibrium points, where point a (the solid dot) is the stable one, since δ can return to this point irrespective of a small disturbance; while point b (the open circle) is the unstable one, since a small disturbance will force δ to depart from this point. Thus, the VSC operates at point a with a power angle of δ_1.

The transient stability issue arises if P is subjected to a sharp drop, which can result from the grid fault with a voltage sag. It should be noted that the voltage sag will downscale the maximum transmissible power between $\mathbf{V}$ and $\mathbf{E}$, which if smaller than P_0, will lead to the loss of equilibrium points. Thus, in practice, it is usually required to reduce P_0 (meanwhile increase Q_0) when the grid voltage sag happens [39], [40]. However, in order to draw the worst case on the transient stability, it is assumed that $P_0 = 1$ p.u. and $Q_0 = 0$ remain unchanged during the grid fault. Depending on the depth of the voltage sag, there will be two scenarios.

In the first scenario, the equilibrium points still exist after the fault. For example, when E drops to 0.6 p.u., the transferred power P is decreased, leading to a higher phase portrait, shown as the dashed line in Fig. 5(a). Although the phase portrait is lifted after the fault, it can still cross zero at points d and e, which are the two equilibrium points (d is the stable one and e is the unstable one). At the fault occurring instant, δ_1 is held while the operating point jumps from a to c.

$$V = \frac{1.5 K_q E \cos \delta - X_g + \sqrt{\left(X_g - 1.5 K_q E \cos \delta \right)^2 + 6 K_q X_g \left(V_0 + K_q Q_0 \right)}}{3 K_q}. \tag{12}$$

$$\dot{\delta} = K_p \left(P_0 - \frac{3}{2} \cdot \frac{E \sin \delta}{X_g} \cdot \frac{1.5 K_q E \cos \delta - X_g + \sqrt{\left(X_g - 1.5 K_q E \cos \delta \right)^2 + 6 K_q X_g \left(V_0 + K_q Q_0 \right)}}{3 K_q} \right). \tag{13}$$

Then, δ starts to increase due to $\dot{\delta} > 0$, which drives the operating point from c to d, shown as the red line with arrows. Once reaching point d, a new steady state is achieved due to $\dot{\delta} = 0$, and δ will stop at δ_2 and never exceed it. This implies a transient response with no *overshoot*, which essentially comes from the first-order nature of the non-inertial grid-forming control schemes. Thanks to this first-order dynamic behavior, the VSC can retain a stable operation as long as there are equilibrium points, where $\dot{\delta} = 0$ can be reached after the transient process.

A violation of this condition will lead to an instability, which is illustrated as the second scenario. As shown in Fig. 5(a), when E further drops to 0.5 p.u., the resultant phase portrait is fully above zero, where no equilibrium points exist. That means, the maximum transmissible power between **V** and **E** cannot reach P_0, and the VSC is definitely unstable. Consequently, δ will diverge to infinite as $\dot{\delta} > 0$ always holds, shown as the green line with arrows. To restore the stable operation, the fault must be cleared to recover the grid voltage so that the equilibrium points can be created. In this case, the fault clearing time becomes critical [22], which is not further studied in this paper due to the space limit. Hence, in the following analysis, the voltage sag with equilibrium points (e.g., E drops to 0.6 p.u.) will be targeted, and the research objective is to drive the VSC to the equilibrium point by optimizing the controller parameters, even without clearing the fault, which, in other words, is to ride through the fault.

It is worth noting that the above discussion is carried out by combining the dynamics of active and reactive power loops into a single differential equation, given in (13). This process allows for a quantitative analysis of the overall system transient behavior, but on the other hand, it gives little insight into the mechanism of how the reactive power control takes effect. To address this issue, the VSC voltage dynamic, which is dominated by the reactive power loop, is intentionally studied here. Based on (12), the V-δ curves are plotted for different grid conditions, as shown in Fig. 5(b). At the fault occurring instant, as E drops suddenly, Q increases sharply referring to (9), which causes V to jump down from point a. Then, as δ increases, Q also increases referring to (9), which causes V to drop following the Q-V droop law. As indicated by the trajectories with arrows, the voltage drop stops at point d for $E = 0.6$ p.u. and continues for $E = 0.5$ p.u.. Recalling (8) and (10), this transient voltage drop will reduce P, which, in turn, enlarges $\dot{\delta}$ and pushes δ to the stability boundary. As a result, the transient stability is weakened. This finding provides a theoretical basis for the transient analysis of inertial grid-forming control schemes, which will be presented in the next section.

IV. TRANSIENT STABILITY OF INERTIAL GRID-FORMING CONTROL — DROOP CONTROL WITH LPFS AND VSG CONTROL

As a second-order system, the inertial grid-forming control schemes, i.e., the droop control with LPFs and the VSG control, have dramatically different transient behaviors compared with the non-inertial ones. These differences are thoroughly explored in this section by a case study on the droop control with LPFs. To show the impacts of the two LPFs individually, the droop controller without an LPF in the reactive power loop is discussed first.

A. An LPF in Active Power Loop Only

Recalling (8) and Fig. 4, the dynamic equation of δ, with an LPF in the active power loop, can be described as

$$
\begin{aligned}
\delta &= \frac{K_p}{s} \cdot \frac{\omega_p}{s+\omega_p} \cdot \left(P_0 - \frac{3}{2} \cdot \frac{EV\sin\delta}{X_g} \right) \\
\Rightarrow \ddot{\delta} &= -\omega_p \dot{\delta} + \omega_p K_p \left(P_0 - \frac{3}{2} \cdot \frac{EV\sin\delta}{X_g} \right)
\end{aligned}
\tag{14}
$$

Since there is no LPF in the reactive power loop ($\omega_q = \infty$), the voltage dynamic stays unchanged as (12), which is substituted into (14), gives rise to (15), shown at the bottom of this page.

Before studying its transient response, the equilibrium points should be clarified first. Although a virtual inertia is introduced by the LPF, it only changes the transient behavior of the VSC, but does not affect the power transfer capability between **V** and **E**. Thus, the system has the same equilibrium points as those in the non-inertial scenario, when subjected to an identical voltage sag. However, as the transient behavior has been changed by the LPF, the VSC may not reach the equilibrium point even if it exists.

Based on (15), the phase portraits when E drops from 1 p.u. to 0.6 p.u. are plotted in Fig. 6(a) with the same parameters in Table I. To provide a comparable basis, the curve without any LPFs ($\omega_p = \omega_q = \infty$), which has been presented in Fig. 5(a), is redrawn with the dashed line. As discussed above, its trajectory starts at the initial equilibrium point a, and jumps to point c when the grid voltage sag occurs, then moves toward the destination equilibrium point d, shown as the red line with arrows. With the LPF in the active power loop (a finite ω_p), the system will behave with a second-order dynamic response. Although the operating point still moves from a to d in a stable operation, the trajectory is different from the non-inertial grid-forming control, shown as the blue line with arrows. During the transient response, δ can exceed its steady-state value δ_2, which implies an overshoot in the power angle.

$$
\ddot{\delta} = -\omega_p \dot{\delta} + \omega_p K_p \left(P_0 - \frac{3}{2} \cdot \frac{E\sin\delta}{X_g} \cdot \frac{1.5K_q E\cos\delta - X_g + \sqrt{\left(X_g - 1.5K_q E\cos\delta\right)^2 + 6K_q X_g \left(V_0 + K_q Q_0\right)}}{3K_q} \right).
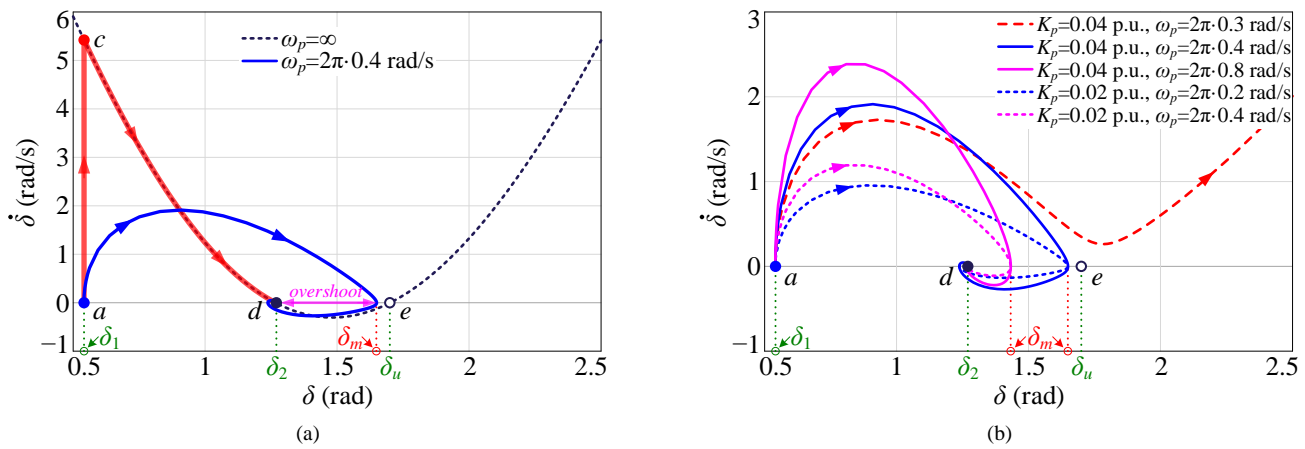\tag{15}
$$

Fig. 6. Phase portraits of the droop control with an LPF in the active power loop only (E = 1 p.u. → 0.6 p.u. and $\omega_q = \infty$). (a) Comparison with the non-inertial one. (b) Influences of controller parameters.

As shown in Fig. 6(a), the power angle overshoot is defined as the difference between the maximum power angle that reached in the transient process, which is denoted by δ_m, and the steady-state power angle δ_2. It is known that for a stable operation, δ_m should not exceed δ_u, i.e., the power angle at the unstable equilibrium point (point e) [22]. To meet this requirement, a smaller overshoot would be desirable.

In the second-order system, the overshoot is determined by its *damping ratio* [44]. A larger damping ratio leads to a smaller overshoot. To quantify the power angle overshoot, the damping ratio of the present control schemes needs to be identified first. For this purpose, the large-signal model in Fig. 4 is simplified by manipulating the nonlinear term G_P as follows

$$P = \frac{3}{2} \cdot \frac{EV}{X_g} \cdot \sin\delta \approx \frac{3}{2} \cdot \frac{EV}{X_g} \cdot \delta \implies G_P \approx \frac{3}{2} \cdot \frac{EV}{X_g}. \quad (16)$$

This approximation is valid in the low-frequency range [10], [21]. Thus, it is useful to evaluate slow dynamic processes, such as the transient behavior under study. From (16), it is clear to see that G_P is a proportional gain for given circuit parameters. Then, recalling Fig. 4, the dynamic of the active power loop can be described in the s-domain as

$$\delta = \frac{K_p}{s} \cdot \frac{\omega_p}{s+\omega_p} \cdot (P_0 - G_P \cdot \delta) \implies \delta = \frac{K_p \omega_p}{s^2 + \omega_p s + K_p \omega_p G_P} P_0. \quad (17)$$

By analogizing with the standard second-order transfer function, the system damping ratio ζ is derived as

$$\zeta = \frac{1}{2}\sqrt{\frac{\omega_p}{K_p G_P}}. \quad (18)$$

Since G_P has been specified by the circuit parameters, ζ will be determined by the ratio of ω_p to K_p, i.e., ω_p/K_p. Its influence on the transient behavior is illustrated in Fig. 6(b).

For different sets of K_p and ω_p yielding the same ω_p/K_p, such as (K_p = 0.04 p.u. and ω_p = 2π·0.4 rad/s) *vs* (K_p = 0.02 p.u. and ω_p = 2π·0.2 rad/s) and (K_p = 0.04 p.u. and ω_p = 2π·0.8 rad/s) *vs* (K_p = 0.02 p.u. and ω_p = 2π·0.4 rad/s), equal overshoots can be readily identified due to their identical ζ. Moreover, the overshoot decreases with the increase of ω_p/K_p, due to the increased ζ. Therefore, a larger ω_p and a smaller K_p are expected to reduce the power angle overshoot and thus to enhance the transient stability. On the contrary, an instability can arise with either a small ω_p or a large K_p (a small ζ). For example, with K_p = 0.04 p.u. and ω_p = 2π·0.3 rad/s, the weakly damped transient response yields δ to exceed δ_u. As a result, δ keeps increasing as $\dot{\delta} > 0$ always holds, which means a loss of synchronization with the grid, as shown in Fig. 6(b).

Considering the equivalence between the droop control with LPFs and the VSG control, the above analysis can be easily extended to the VSG. Recalling (7), ζ in the VSG control can be obtained as

$$\zeta = \frac{D_p}{2\sqrt{JG_P}}. \quad (19)$$

Consequently, a smaller J and a larger D_p are helpful to improve the transient stability of the VSC. These findings provide not only a useful rule to design the controller parameters but also a new perspective on the virtual inertia. While the virtual inertia improves the system frequency stability [12], [13], it degrades the transient stability by raising the system order. Unlike the non-inertial VSC (a first-order system) where a stable operation can be retained as long as there are equilibrium points, the inertial VSC (a second-order system) can still be destabilized even if the equilibrium points exist, due to the lack of damping.

B. LPFs in Both Active and Reactive Power Loops

Based on the above analysis, the impact of LPF in the reactive power loop is further investigated. With the LPF, the dynamic of the reactive power loop is changed into
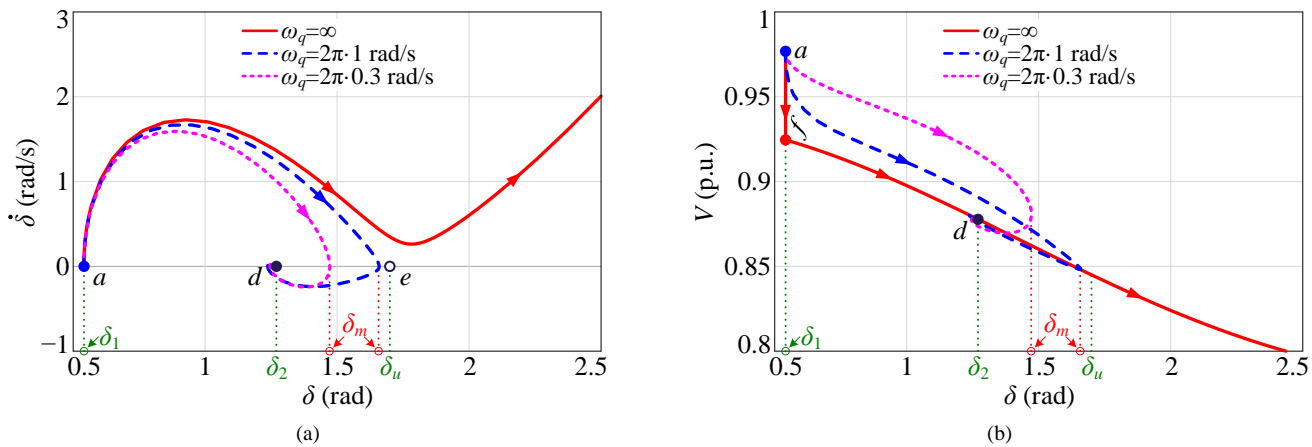
Fig. 7. (a) Phase portraits and (b) V-δ curves of the droop control with LPFs in both active and reactive power loops ($E = 1$ p.u. → 0.6 p.u., $K_p = 0.04$ p.u., and $\omega_p = 2\pi\cdot0.3$ rad/s).

$$V = V_0 + K_q \cdot \frac{\omega_q}{s + \omega_q} \cdot \left(Q_0 - \frac{3}{2} \cdot \frac{V^2 - EV\cos\delta}{X_g}\right)$$
$$\Rightarrow \dot{V} = -\omega_q V + \omega_q V_0 + \omega_q K_q \left(Q_0 - \frac{3}{2} \cdot \frac{V^2 - EV\cos\delta}{X_g}\right) \tag{20}$$

Unlike the quadratic equation in (11), Eq. (20) is a differential equation. It is thus difficult to acquire an explicit expression of V [like (12)] from this differential equation. Fortunately, we can use the MATLAB command "ode45" to solve differential equations in (14) and (20) together, and then plot the phase portraits and the V-δ curves, as shown in Fig. 7. In this study, the voltage sag from 1 p.u. to 0.6 p.u. is still targeted, $K_p = 0.04$ p.u. and $\omega_p = 2\pi\cdot0.3$ rad/s are fixed, and the unstable response without the LPF ($\omega_q = \infty$) is redrawn with the solid line for comparison. By adding the LPF (a finite ω_q), the system trajectory converges to the equilibrium point d, implying a stable response. Moreover, as ω_q goes lower, the system trajectory is shifted inward with a smaller power angle overshoot, as shown in Fig. 7(a). Therefore, a smaller ω_q leads to a better transient stability.

To reveal the underlying mechanism, the VSC voltage dynamic is further analyzed. As interpreted in Section III, the reactive power loop imposes a negative effect on the transient response by generating a voltage drop. Such an effect is revisited in Fig. 7(b). For $\omega_q = \infty$ (no LPF), V jumps from the initial point a to point f when the grid voltage sag occurs. Then, as δ increases, V continues to drop following the Q-V droop law. This transient voltage drop is alleviated by the LPF, which slows down the dynamic of the reactive power loop and makes V insensitive to the variation of Q. Consequently, during the transient process, the VSC voltage is raised with the decrease of ω_q, as shown with the dashed lines. The raised V helps to increase P and diminish $\dot{\delta}$ and then push δ lower than δ_u, which restores the synchronization with the grid. Accordingly, V declines slowly from point a and finally stops at point d.
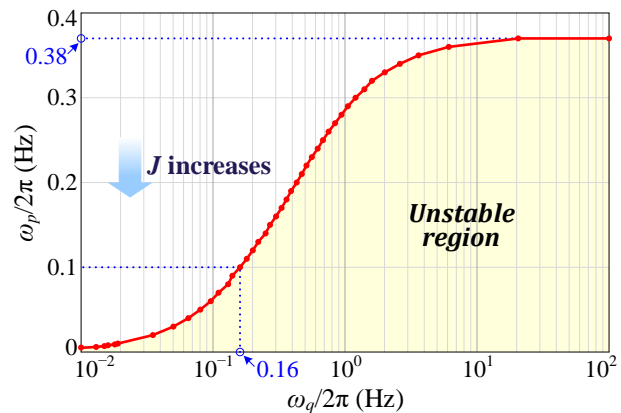

Fig. 8. Stability boundary regarding ω_p versus ω_q when E drops from 1 p.u. to 0.6 p.u. ($K_p = 0.04$ p.u.).

From the above analysis, it can be concluded that the two LPFs in the active and the reactive power loops take opposite effects on the transient stability: the former degrades the stability while the latter improves it. The strong transient stability demands a fast LPF with a high cutoff frequency (a low inertia) in the active power loop and a slow LPF with a low cutoff frequency in the reactive power loop. These findings will be fully validated by experimental results in the next section.

C. Stabilizing High-Inertia Grid-Forming VSC

An important issue needs to be concerned that there is a conflict between the frequency stability and the transient stability in terms of the virtual inertia. Although unexpected from the transient stability perspective, a high inertia is usually emulated in the VSC to support the system frequency. Hence, there is an urgent demand to stabilize the high-inertia grid-forming VSC.

Recalling (19), a large J destabilizes the VSC by decreasing ζ. Thus, a natural idea for the stability improvement comes to mind is to increase ζ by enlarging D_p. As depicted in (7), $J = 1/(\omega_p K_p)$ and $D_p = 1/K_p$. Therefore, for a given J (a given product of ω_p and K_p), it is desirable to configure a larger ω_p and a smaller K_p in order to increase ζ.
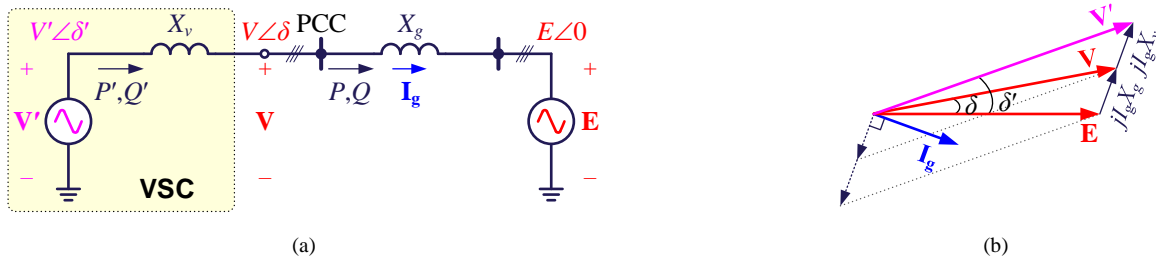
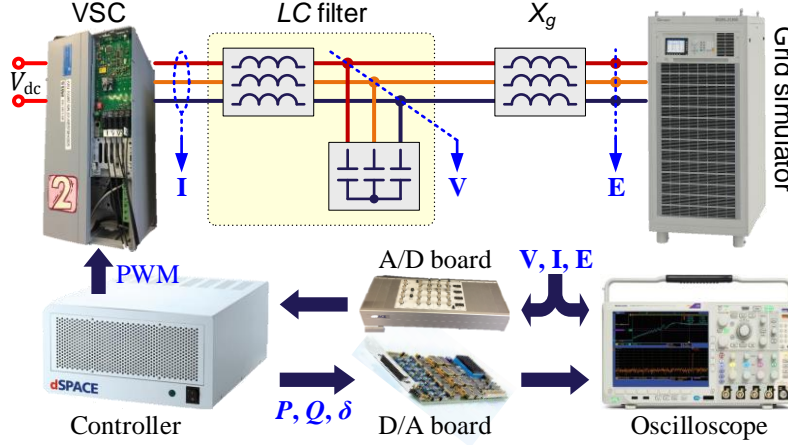Fig. 9. (a) Simplified circuit and (b) phasor diagram of the grid-forming VSC with virtual impedance control.

Fig. 10. Configuration of the experimental setup.

Except for increasing ζ, the transient stability can also be enhanced by decreasing ω_q, as discussed above. Taking $K_p = 0.04$ p.u. as an instance, the design rule of ω_q in the high-inertia case is derived. As K_p has been specified, J is now solely determined by ω_p. For every specific ω_p, the critical value of ω_q for a stable operation can be found by trial and error. These critical points are shown as solid dots in Fig. 8, where ω_q is depicted in log scale for convenience of observation. Connecting the critical points into a line yields the stability boundary, below which is the unstable region, shown as the shaded area. It can be seen that with the increase of J, the maximum allowed ω_q in the stable region decreases. For example, if $\omega_p = 2\pi \cdot 0.1$ rad/s is set, then $\omega_q \leq 2\pi \cdot 0.16$ rad/s must be adopted, as identified in Fig. 8. By lowering ω_q, a higher inertia becomes viable. Hence, combining the flexible configuration of K_p, ω_p, and ω_q, it is now possible for the grid-forming VSC to guarantee both the frequency stability and the transient stability.

D. Influence of Virtual Impedance Control

In the previous analysis, the grid-forming VSC is modeled as an ideal voltage source **V** without any internal impedance [see Fig. 3(a)], due to its superior voltage tracking ability. However, in some applications, an internal impedance is intentionally introduced to the VSC by the virtual impedance control [45], [46]. In this scenario, the VSC is equivalent to a voltage source **V'** in series with a virtual impedance X_v, which is mainly inductive, as shown in Fig. 9(a). Consequently, the total line impedance becomes $X_v + X_g$, and the phasor diagram is given in Fig. 9(b). It is noted that $\mathbf{V'} = V' \angle \delta'$, where V' is the internal voltage amplitude, and δ' denotes the phase

TABLE I
NOMINAL PARAMETERS OF THE EXPERIMENTAL SETUP

Parameter	Value	p.u.	Parameter	Value	p.u.
Rated active power P_0	2 kW	1.0	Rated reactive power Q_0	0	0
Rated voltage V_0	100 V	1.0	Filter inductance L_f	1.5 mH	0.06
Grid voltage E	100 V	1.0	Filter capacitance C_f	20 μF	0.05
Grid frequency ω_0	314 rad/s		Grid inductance L_g	12 mH	0.5
P-f droop gain K_p	$0.04\omega_0/P_{max}$	0.04	Q-V droop gain K_q	$0.1V_0/Q_{max}$	0.1

difference between **V'** and **E**, which is defined as the virtual power angle. The transient response of the VSC can then be characterized by the virtual state variables V' and δ', with X_v being regarded as a part of the grid impedance. In this way, the previous analysis can be extended to the VSC with virtual impedance control by replacing V, δ, and X_g with V', δ', and $X_v + X_g$, whose effectiveness will be verified by experimental results in the next section.

V. EXPERIMENTAL VERIFICATION

To verify the theoretical analysis, an experimental setup, as shown in Fig. 10, is built and tested in the lab. The VSC is implemented by a Danfoss VLT FC-103P11K inverter, whose input is supplied by a constant dc voltage source, and its output is connected with an *LC* filter. A three-phase inductor is used to emulate the grid impedance X_g. The Chroma 61845 grid simulator is employed to provide the grid voltage **E**. The

TABLE II
CONTROLLER PARAMETERS FOR THE EXPERIMENTAL TEST

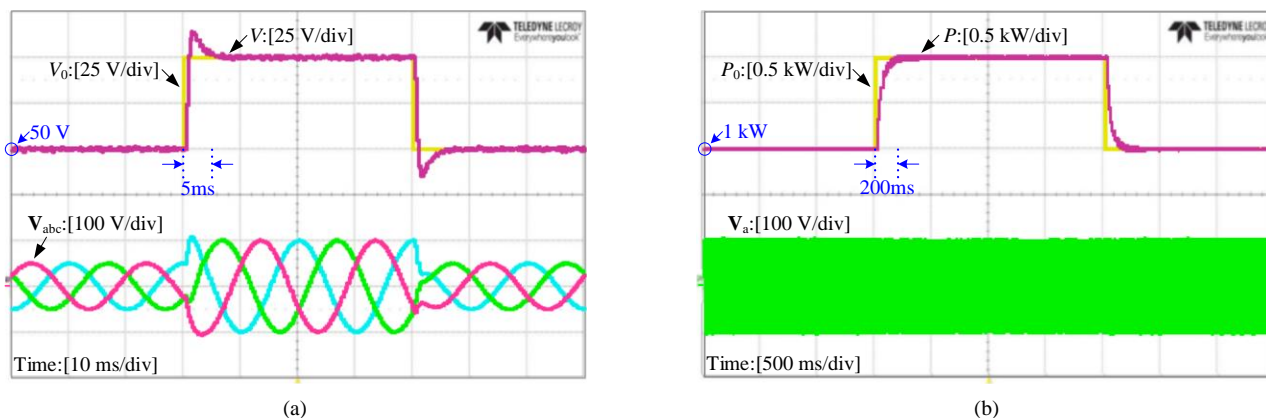| Parameter	Case I	Case II-A	Case II-B	Case II-C	Case II-D	Case III-A	Case III-B	Case III-C	Case III-D
K_p	0.04 p.u.	0.04 p.u.	0.02 p.u.	0.04 p.u.	0.04 p.u.	0.04 p.u.	0.04 p.u.	0.04 p.u.	0.04 p.u.
K_q	0.1 p.u.	0.1 p.u.	0.1 p.u.	0.1 p.u.	0.1 p.u.	0.1 p.u.	0.1 p.u.	0.1 p.u.	0.1 p.u.
ω_p	∞	2π·0.4rad/s	2π·0.2rad/s	2π·0.8rad/s	2π·0.3rad/s	2π·0.3rad/s	2π·0.3rad/s	2π·0.1rad/s	2π·0.1rad/s
ω_q	∞	∞	∞	∞	∞	2π·1rad/s	2π·0.3rad/s	2π·0.3rad/s	2π·0.1rad/s

Fig. 11. Experimental step responses of (a) inner dual-loop voltage control and (b) outer power control of the grid-forming VSC.

multi-loop control architecture, which has the dedicated voltage and current control loops, is adopted as the test benchmark. The VSC output voltage **V** and output current **I** are measured through the dSPACE DS2004 A/D board. The measured signals are sent to the dSPACE DS1007 platform to implement the outer power control and the inner dual-loop voltage control. The phase angles of **V** and **E** are measured by a fast PLL, and their phase difference, which is denoted as the power angle δ, is fed to the oscilloscope through the dSPACE DS2102 D/A board.

Table I gives the nominal parameters of the experimental setup. A low grid voltage $E = 100$ V is intentionally chosen for the convenience of emulating the low short-circuit-ratio grid condition. The droop gains K_p and K_q are designed according to the frequency/voltage regulation demands in grid codes [21], which specify the allowed frequency deviation $\Delta\omega$ under the maximum active power P_{max} and the allowed voltage deviation ΔV under the maximum reactive power Q_{max}. For the grid-connected application, the VSC can inject the full active power or the full reactive power depending on the operating scenarios. Hence, $P_{max} = Q_{max} = 1$ p.u.. Meanwhile, $\Delta\omega = 0.04\omega_0$ and $\Delta V = 0.1V_0$ are set, which give rise to $K_p = 0.04\omega_0/P_{max}$ and $K_q = 0.1V_0/Q_{max}$.

To perform a comparative test, the basic droop control and the droop control with LPFs are taken to represent the non-inertial and the inertial grid-forming control schemes, respectively. Moreover, different sets of controller parameters are examined, and they are grouped into three cases, as shown in Table II. Case I, Case II, and Case III refer to 1) the basic droop control, 2) the droop control with an LPF in the active power loop only, and 3) the droop control with LPFs in both

active and reactive power loops, respectively. In particular, K_p in Case II-B is adjusted from its nominal value for an intentional test, which will be shown later. Based on these parameters, transient responses of the VSC are examined in the case of the grid voltage sag.

First, multiple-timescale control dynamics of the grid-forming VSC are tested. Fig. 11(a) gives a step response of the inner dual-loop voltage control. In this test, the VSC is disconnected from the grid and controlled by the inner voltage and current loop (no outer power loop). When the voltage reference V_0 steps between 50 V and 100 V, the VSC voltage amplitude V can fast track this reference change with a settling time of 5 ms. Fig. 11(b) gives a step response of the outer power control loop, where the VSC is connected to the grid with the basic droop control. When the active power reference P_0 steps between 1 kW and 2 kW, V is almost unchanged while a settling time of 200 ms is observed in the output active power. The settling time can be even longer if the inertial grid-forming control is employed, due to the effect of the LPF. The experimental results show decoupled timescales between the inner voltage & current loop and the outer power loop, which justifies the assumption in Section II that the inner dual-loop voltage control can be treated as a unity gain with an ideal reference tracking.

Then, transient responses of the VSC under the grid voltage sag are tested. The active power P, the reactive power Q, and the power angle δ are calculated. The waveform of the VSC output current I is displayed. For the better clarity, the grid voltage amplitude E and the VSC voltage amplitude V, rather than their waveforms, are measured and displayed. Fig. 12 shows experimental results acquired with the basic droop
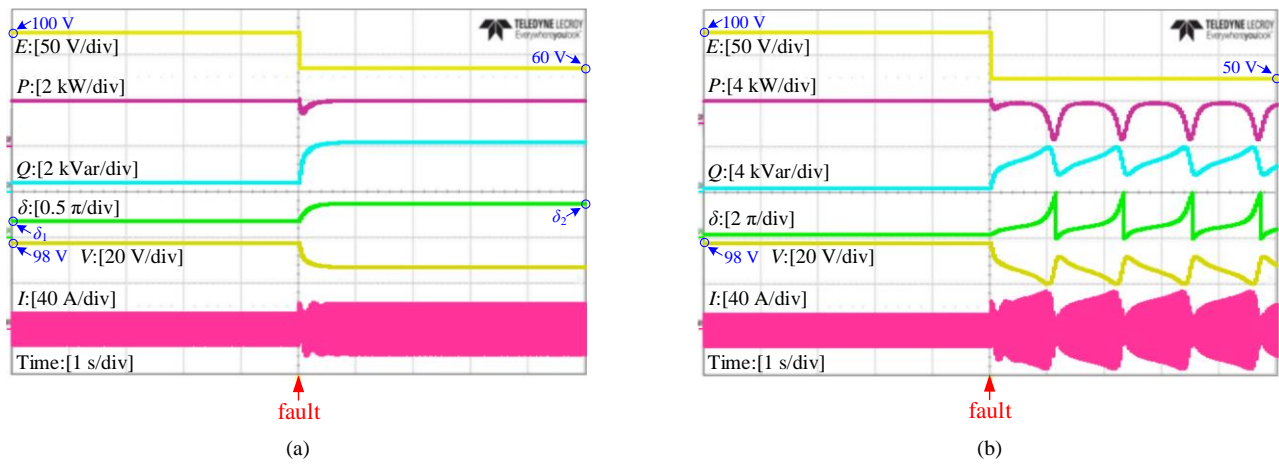
Fig. 12. Experimental transient responses of the basic droop control with controller parameters in Case I ($K_p = 0.04$ p.u., $K_q = 0.1$ p.u., and $\omega_p = \omega_q = \infty$). (a) E drops to 0.6 p.u.. (b) E drops to 0.5 p.u..
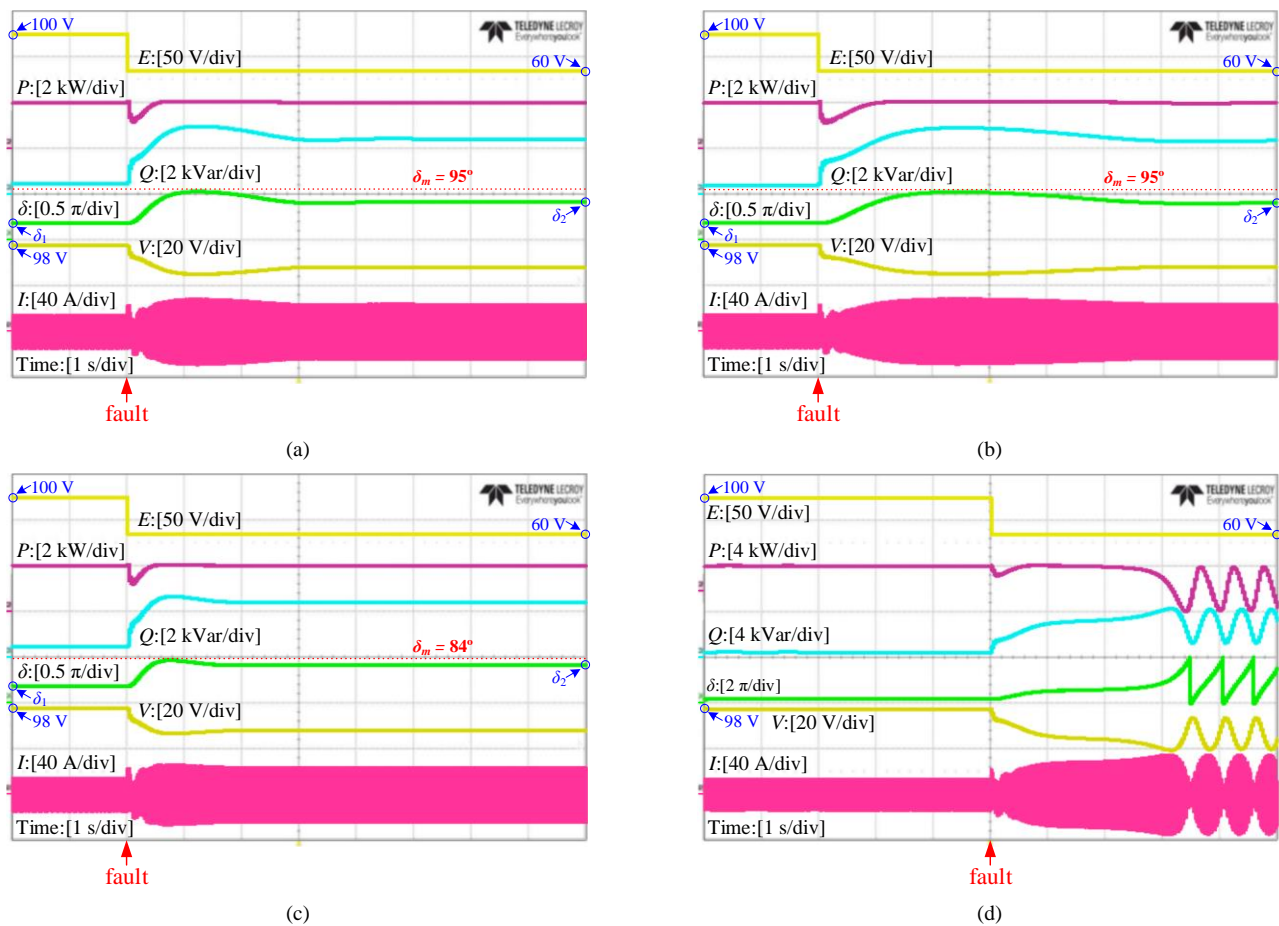

Fig. 13. Experimental transient responses of the droop control with an LPF in the active power loop only (when E drops to 0.6 p.u.). (a) Case II-A: $K_p = 0.04$ p.u., $K_q = 0.1$ p.u., $\omega_p = 2\pi \cdot 0.4$ rad/s, and $\omega_q = \infty$. (b) Case II-B: $K_p = 0.02$ p.u., $K_q = 0.1$ p.u., $\omega_p = 2\pi \cdot 0.2$ rad/s, and $\omega_q = \infty$. (c) Case II-C: $K_p = 0.04$ p.u., $K_q = 0.1$ p.u., $\omega_p = 2\pi \cdot 0.8$ rad/s, and $\omega_q = \infty$. (d) Case II-D: $K_p = 0.04$ p.u., $K_q = 0.1$ p.u., $\omega_p = 2\pi \cdot 0.3$ rad/s, and $\omega_q = \infty$.

control, where controller parameters in Case I are adopted. When E drops to 0.6 p.u., there are equilibrium points after the fault. As shown in Fig. 12(a), δ starts to increase gradually and reaches a new steady state without any overshoot, which confirms a first-order dynamic behavior. The power angles before and after the fault are 30º and 70º, respectively, which correspond to δ_1 and δ_2 in Fig. 5(a). However, when E drops to 0.5 p.u., the equilibrium points no longer exist, and the active power delivered to the grid cannot reach P_0. As shown

in Fig. 12(b), low-frequency oscillations are triggered in the waveforms of P, Q, δ, V, and I, which imply an instability and agree with the analysis in Section III.

For the inertial grid-forming control, experiments when E drops to 0.6 p.u. are performed with different parameter settings. Although the equilibrium points still exist after the fault, they may not be reached due to the inertial transient response. First, the LPF in the active power loop is enabled with controller parameters in Case II. As shown in Fig. 13,
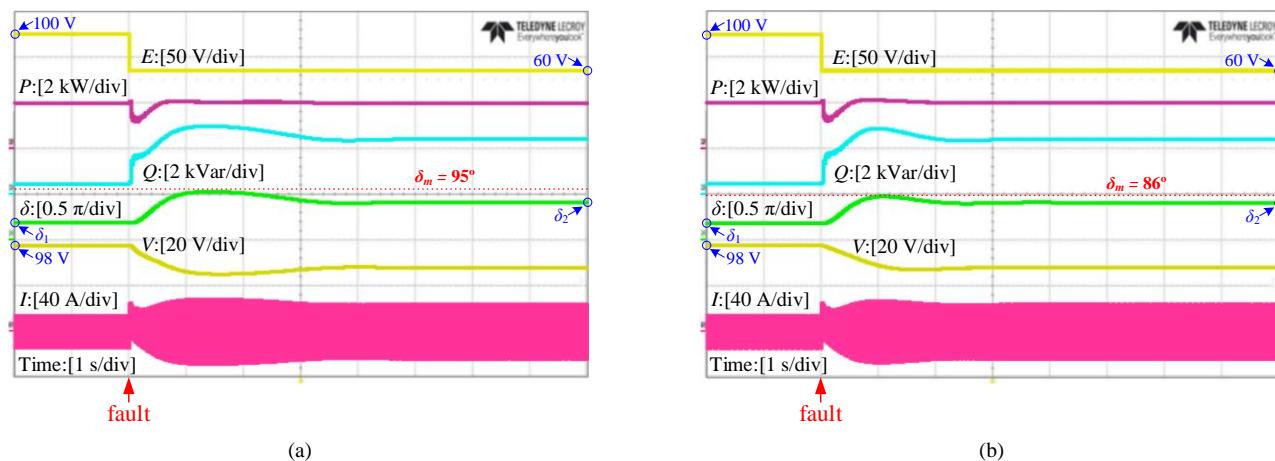
This article has been accepted for publication in a future issue of this journal, but has not been fully edited. Content may change prior to final publication. Citation information: DOI 10.1109/JESTPE.2019.2946310, IEEE Journal of Emerging and Selected Topics in Power Electronics

IEEE JOURNAL OF EMERGING AND SELECTED TOPICS IN POWER ELECTRONICS 12

Fig. 14. Experimental transient responses of the droop control with LPFs in both active and reactive power loops (when E drops to 0.6 p.u.). (a) Case III-A: K_p = 0.04 p.u., K_q = 0.1 p.u., ω_p = 2π·0.3 rad/s, and ω_q = 2π·1 rad/s. (b) Case III-B: K_p = 0.04 p.u., K_q = 0.1 p.u., ω_p = 2π·0.3 rad/s, and ω_q = 2π·0.3 rad/s.
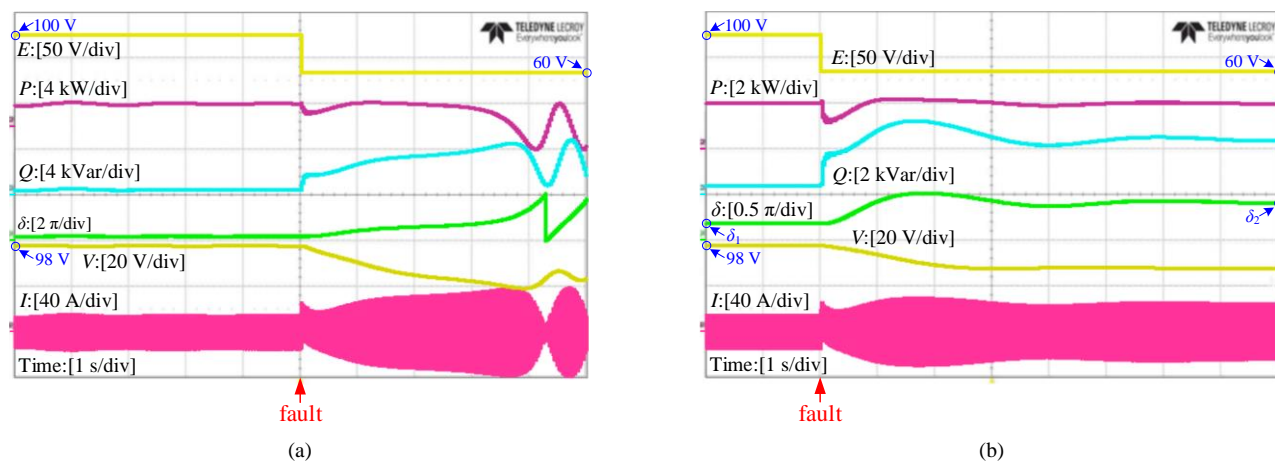

Fig. 15. Experimental transient responses of the high-inertia grid-forming VSC (when E drops to 0.6 p.u.). (a) Case III-C: K_p = 0.04 p.u., K_q = 0.1 p.u., ω_p = 2π·0.1 rad/s, and ω_q = 2π·0.3 rad/s. (b) Case III-D: K_p = 0.04 p.u., K_q = 0.1 p.u., ω_p = 2π·0.1 rad/s, and ω_q = 2π·0.1 rad/s.

power angle overshoots are observed in their transient responses, where δ increases to its maximum value δ_m first and then declines to the steady-state value δ_2. These verify a second-order dynamic response as expected in Section IV-A. In Case II-A (K_p = 0.04 p.u. and ω_p = 2π·0.4 rad/s) and Case II-B (K_p = 0.02 p.u. and ω_p = 2π·0.2 rad/s), as shown in Figs. 13(a) and 13(b), an equal δ_m = 95° is measured due to their identical ω_p/K_p (an identical ζ); while in Case II-C (K_p = 0.04 p.u. and ω_p = 2π·0.8 rad/s), as shown in Fig. 13(c), δ_m is reduced to 84° due to the increased ω_p/K_p. On the contrary, a decrease of ω_p/K_p, which is realized by decreasing ω_p, is tested in Case II-D (K_p = 0.04 p.u. and ω_p = 2π·0.3 rad/s). As shown in Fig. 13(d), an unstable transient response, which is similar to Fig. 12(b), is triggered by the fault. However, unlike Figs. 12(b) where the transient instability is caused by the absence of equilibrium points, the instability in Fig. 13(d) results from the lack of damping which fails to drive the VSC to the existing equilibrium point.

Such an instability can be removed by incorporating a slow LPF into the reactive power loop, as illustrated in Section IV-B. For verification, ω_q = 2π·1 rad/s (Case III-A) and ω_q = 2π·0.3 rad/s (Case III-B) are tested on the basis of K_p = 0.04 p.u. and ω_p = 2π·0.3 rad/s, as shown in Figs. 14(a) and 14(b). It can be seen that as ω_q decreases, V is raised during the

transient process, which thus helps to reduce the power angle overshoot. Consequently, δ_m = 95° and δ_m = 86° are measured in the two cases.

Furthermore, the grid-forming VSC is intentionally tested in the high-inertia scenario. Recalling J = 1/($\omega_p K_p$), the high inertia is emulated by further decreasing ω_p to 2π·0.1 rad/s while keeping K_p = 0.04 p.u.. Besides, two different ω_q are comparatively evaluated. With ω_q = 2π·0.3 rad/s (Case III-C), the unstable transient response arises when E drops to 0.6 p.u., as shown in Fig. 15(a). To support the high-inertia operation, one solution is to reconfigure K_p and ω_p to obtain a larger damping ratio. With the same product of K_p and ω_p (the same J), K_p = 0.02 p.u. and ω_p = 2π·0.2 rad/s can be chosen, as those in Case II-B. Its stable operation has been given in Fig. 13(b), which proves an improved transient stability even with ω_q = ∞. The other solution is to decrease ω_q. Keeping K_p = 0.04 p.u. and ω_p = 2π·0.1 rad/s, ω_q ≤ 2π·0.16 rad/s is suggested in Section IV-C. Here, ω_q = 2π·0.1 rad/s (Case III-D) is tested, and its stable operation is shown in Fig. 15(b).

Finally, the grid-forming VSC with virtual impedance control is tested. In this study, a virtual impedance X_v = 0.1 p.u. is emulated, and X_g is reduced to 0.4 p.u. accordingly to keep the total line impedance X_v + X_g unchanged. The measured results are shown in Fig. 16, where the controller
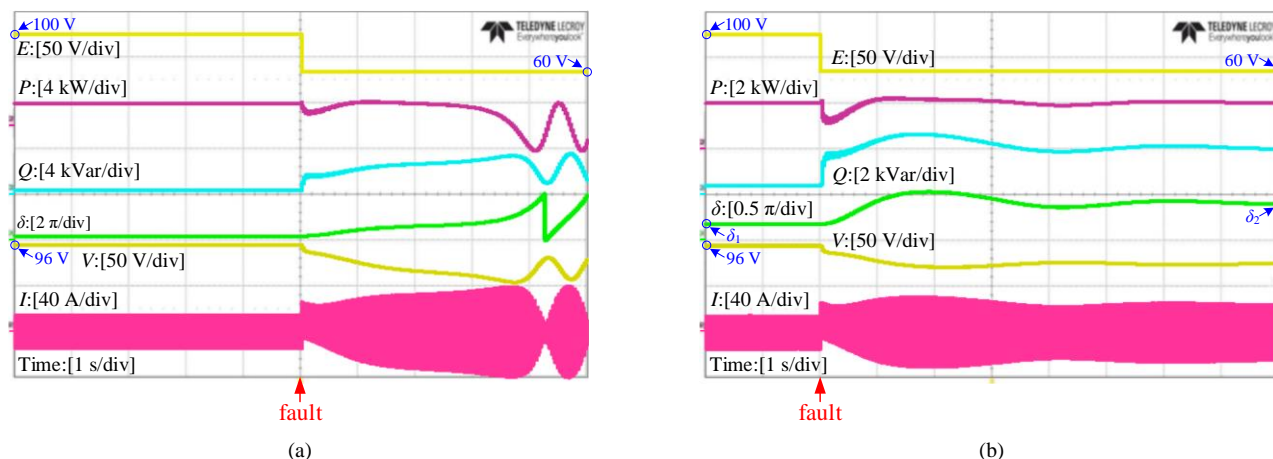
Fig. 16. Experimental transient responses of the grid-forming VSC with virtual impedance control (when E drops to 0.6 p.u.). (a) Case III-C: $K_p = 0.04$ p.u., $K_q = 0.1$ p.u., $\omega_p = 2\pi \cdot 0.1$ rad/s, and $\omega_q = 2\pi \cdot 0.3$ rad/s. (b) Case III-D: $K_p = 0.04$ p.u., $K_q = 0.1$ p.u., $\omega_p = 2\pi \cdot 0.1$ rad/s, and $\omega_q = 2\pi \cdot 0.1$ rad/s.

parameters in Case III-C and Case III-D are taken for comparison. It can be seen that similar transient responses with those in Fig. 15 are obtained in the two cases. Moreover, it is worth noting that V drops deeper than those in Fig. 15 during the transient processes, due to the smaller X_g between V and E. These experimental results confirm the theoretical analysis on the influence of the virtual impedance control.

VI. CONCLUSION

This paper has explored the transient stability of grid-forming VSCs. Four typical grid-forming control schemes, namely the PSC, the basic droop control, the droop control with LPFs, and the VSG control, have been revisited and classified into the non-inertial grid-forming control and the inertial grid-forming control. A general large-signal model that accounts for the coupling between the active and the reactive power loops has been developed to characterize their dynamics. Based on which, transient stabilities of different control schemes are comparatively evaluated using the phase portrait. The main findings are summarized as follows.

1) Owing to the first-order nature, the PSC and the basic droop control (the non-inertial grid-forming control) can retain a stable operation as long as there are equilibrium points, while the second-order dynamic behavior of the droop control with LPFs and the VSG control (the inertial grid-forming control) can be destabilized even if the equilibrium points exist, due to the lack of damping. From the transient stability perspective, the non-inertial grid-forming control is more competitive.

2) In the case of the inertial grid-forming control, controller design guidelines are proposed to enhance the system damping as well as the transient stability. A small droop gain and a fast LPF with a high cutoff frequency (a low inertia) have been found critical for the active power loop. Yet, for the reactive power loop, a slow LPF with a low cutoff frequency can alleviate the undesired transient voltage drop and thus improve the transient stability.

3) Combining the flexible configuration of the P-f droop gain and the LPFs' cutoff frequencies, it is possible for

the high-inertia grid-forming VSC to guarantee both the frequency stability and the transient stability.

Except for the four typical control schemes, the analytical method developed in this paper can also be used to characterize the transient behaviors for more sophisticated grid-forming operations, which is considered to be our future work.

REFERENCES

[1] D. Pan, X. Ruan, C. Bao, W. Li, and X. Wang, "Capacitor-current-feedback active damping with reduced computation delay for improving robustness of *LCL*-type grid-connected inverter," *IEEE Trans. Power Electron.*, vol. 29, no. 7, pp. 3414−3427, Jul. 2014.

[2] D. Pan, X. Ruan, C. Bao, W. Li, and X. Wang, "Optimized controller design for *LCL*-type grid-connected inverter to achieve high robustness against grid-impedance variation," *IEEE Trans. Ind. Electron.*, vol. 62, no. 3, pp. 1537−1547, Mar. 2015.

[3] D. Pan, X. Ruan, X. Wang, H. Yu, and Z. Xing, "Analysis and design of current control schemes for *LCL*-type grid-connected inverter based on a general mathematical model," *IEEE Trans. Power Electron.*, vol. 32, no. 6, pp. 4395−4410, Jun. 2017.

[4] M. E. Elkhatib, W. Du, and R. H. Lasseter, "Evaluation of inverter-based grid frequency support using frequency-watt and grid-forming PV inverters," in *Proc. IEEE Power & Energy Society General Meeting*, Portland, OR, USA, Aug. 2018.

[5] U. Markovic, O. Stanojev, P. Aristidou, and G. Hug, "Partial grid forming concept for 100% inverter-based transmission systems," in *Proc. IEEE Power & Energy Society General Meeting*, Portland, OR, USA, Aug. 2018.

[6] J. Rocabert, A. Luna, F. Blaabjerg, and P. Rodríguez, "Control of power converters in AC microgrids," *IEEE Trans. Power Electron.*, vol. 27, no. 11, pp. 4734−4749, Nov. 2012.

[7] F. Milano, F. Dörfler, G. Hug, D. J. Hill, and G. Verbič, "Foundations and challenges of low-inertia systems," in *Proc. Power Systems Computation Conference (PSCC)*, Dublin, Ireland, Jun. 2018.

[8] Y. W. Li, D. M. Vilathgamuwa, and P. C. Loh, "Design, analysis, and real-time testing of a controller for multibus microgrid system," *IEEE Trans. Power Electron.*, vol. 19, no. 5, pp. 1195−1204, Sep. 2004.

[9] J. M. Guerrero, L. G. de Vicuña, J. Matas, M. Castilla, and J. Miret, "A wireless controller to enhance dynamic performance of parallel inverters in distributed generation systems," *IEEE Trans. Power Electron.*, vol. 19, no. 5, pp. 1205−1213, Sep. 2004.

[10] L. Zhang, L. Harnefors, and H.-P. Nee, "Power-synchronization control of grid-connected voltage-source converters," *IEEE Trans. Power Syst.*, vol. 25, no. 2, pp. 809−820, May 2010.

[11] L. Zhang, L. Harnefors, and H.-P. Nee, "Interconnection of two very weak AC systems by VSC-HVDC links using power-synchronization control," *IEEE Trans. Power Syst.*, vol. 26, no. 1, pp. 344−355, Feb. 2011.

This article has been accepted for publication in a future issue of this journal, but has not been fully edited. Content may change prior to final publication. Citation information: DOI 10.1109/JESTPE.2019.2946310, IEEE Journal of Emerging and Selected Topics in Power Electronics

IEEE JOURNAL OF EMERGING AND SELECTED TOPICS IN POWER ELECTRONICS   14

[12] J. Fang, H. Li, Y. Tang, and F. Blaabjerg, "Distributed power system virtual inertia implemented by grid-connected power converters," *IEEE Trans. Power Electron.*, vol. 33, no. 10, pp. 8488−8499, Oct. 2018.

[13] J. Fang, H. Li, Y. Tang, and F. Blaabjerg, "On the inertia of future more-electronics power systems," *IEEE J. Emerg. Sel. Topics Power Electron.*, in press, DOI: 10.1109/JESTPE.2018.2877766.

[14] H.-P. Beck and R. Hesse, "Virtual synchronous machine," in *Proc. 9th International Conference on Electrical Power Quality and Utilisation*, Barcelona, Spain, Oct. 2007.

[15] J. Driesen and K.Visscher, "Virtual synchronous generators," in *Proc. IEEE Power & Energy Society General Meeting*, Pittsburgh, PA, USA, Jul. 2008.

[16] Q.-C. Zhong and G. Weiss, "Synchronverters: inverters that mimic synchronous generators," *IEEE Trans. Ind. Electron.*, vol. 58, no. 4, pp. 1259−1267, Apr. 2011.

[17] Q.-C. Zhong, P.-L. Nguyen, Z. Ma, and W. Sheng, "Self-synchronized synchronverters: inverters without a dedicated synchronization unit," *IEEE Trans. Power Electron.*, vol. 29, no. 2, pp. 617−630, Feb. 2014.

[18] S. D'Arco and J. A. Suul, "Equivalence of virtual synchronous machines and frequency- droops for converter-based microgrids," *IEEE Trans. Smart Grid*, vol. 5, no. 1, pp. 394−395, Jan. 2014.

[19] J. Liu, Y. Miura, and T. Ise, "Comparison of dynamic characteristics between virtual synchronous generator and droop control in inverter-based distributed generators," *IEEE Trans. Power Electron.*, vol. 31, no. 5, pp. 3600−3611, May 2016.

[20] N. Pogaku, M. Prodanović, and T. C. Green, "Modeling, analysis and testing of autonomous operation of an inverter-based microgrid," *IEEE Trans. Power Electron.*, vol. 22, no. 2, pp. 613−625, Mar. 2007.

[21] H. Wu, X. Ruan, D. Yang, X. Chen, W. Zhao, Z. Lv, and Q.-C. Zhong, "Small-signal modeling and parameters design for virtual synchronous generators," *IEEE Trans. Ind. Electron.*, vol. 63, no. 7, pp. 4292−4303, Jul. 2016.

[22] P. Kundur, *Power System Stability and Control*. New York, NY, USA: McGraw-Hill, 1994.

[23] H. Xin, L. Huang, L. Zhang, Z. Wang, and J. Hu, "Synchronous instability mechanism of P-f droop-controlled voltage source converter caused by current saturation," *IEEE Trans. Power Syst.*, vol. 31, no. 6, pp. 5206−5207, Nov. 2016.

[24] L. Huang, H. Xin, Z. Wang, L. Zhang, K. Wu, and J. Hu, "Transient stability analysis and control design of droop-controlled voltage source converters considering current limitation," *IEEE Trans. Smart Grid*, vol. 10, no. 1, pp. 578−591, Jan. 2019.

[25] H. Wu and X. Wang, "Design-oriented transient stability analysis of grid-connected converters with power synchronization control," *IEEE Trans. Ind. Electron.*, vol. 66, no. 8, pp. 6473−6482, Aug. 2019.

[26] P. Hart and B. Lesieutre, "Energy function for a grid-tied, droop-controlled inverter," in *Proc. North American Power Symposium (NAPS)*, Pullman, WA, USA, Sep. 2014.

[27] Z. Shuai, C. Shen, X. Liu, Z. Li, and Z. J. Shen, "Transient angle stability of virtual synchronous generators using Lyapunov's direct method," *IEEE Trans. Smart Grid*, vol. 10, no. 4, pp. 4648−4661, Jul. 2019.

[28] S. Liu and R. A. Dougal, "Dynamic multiphysics model for solar array," *IEEE Trans. Energy Convers.*, vol. 17, no. 2, pp. 285−294, Jun. 2002.

[29] B. Wu, Y. Lang, N. Zargari, and S. Kouro, *Power Conversion and Control of Wind Energy Systems*. New York, NY, USA: Wiley, 2011.

[30] M. K.-Ghartemani, S. A. Khajehoddin, P. Piya, and M. Ebrahimi, "Universal controller for three-phase inverters in a microgrid," *IEEE J. Emerg. Sel. Topics Power Electron.*, vol. 4, no. 4, pp. 1342−1353, Dec. 2016.

[31] P. Piya, M. Ebrahimi, M. K.-Ghartemani, and S. A. Khajehoddin, "Fault ride-through capability of voltage-controlled inverters," *IEEE Trans. Ind. Electron.*, vol. 65, no. 10, pp. 7933−7943, Oct. 2018.

[32] H. Yuan, X. Yuan, and J. Hu, "Modeling of grid-connected VSCs for power system small-signal stability analysis in DC-link voltage control timescale," *IEEE Trans. Power Syst.*, vol. 32, no. 5, pp. 3981−3991, Sep. 2017.

[33] O. Mo, S. D'Arco, and J. A. Suul, "Evaluation of virtual synchronous machines with dynamic or quasi-stationary machine models," *IEEE Trans. Ind. Electron.*, vol. 64, no. 7, pp. 5952−5962, Jul. 2017.

[34] S. A. Khajehoddin, M. K.-Ghartemani, and M. Ebrahimi, "Grid-supporting inverters with improved dynamics," *IEEE Trans. Ind. Electron.*, vol. 66, no. 5, pp. 3655−3667, May 2019.

[35] M. Ebrahimi, S. A. Khajehoddin, and M. K.-Ghartemani, "An improved damping method for virtual synchronous machines," *IEEE Trans. Sustain. Energy*, vol. 10, no. 3, pp. 1491−1500, Jul. 2019.

[36] L. Harnefors, M. Hinkkanen, U. Riaz, F. M. M. Rahman, and L. Zhang, "Robust analytic design of power-synchronization control," *IEEE Trans. Ind. Electron.*, vol. 66, no. 8, pp. 5810−5819, Aug. 2019.

[37] P. Cairoli and R. A. Dougal, "Fault detection and isolation in medium-voltage DC microgrids: coordination between supply power converters and bus contactors," *IEEE Trans. Power Electron.*, vol. 33, no. 5, pp. 4535−4546, May 2018.

[38] Ö. Göksu, N. A. Cutululis, and P. Sørensen, "Analysis of HVDC and wind turbine converter response during offshore asymmetrical faults," in *Proc. 17th Wind Integration Workshop*, Stockholm, Sweden, Oct. 2018.

[39] Ö. Göksu, "Control of wind turbines during symmetrical and asymmetrical grid faults," Ph. D. dissertation, Aalborg University, Aalborg, Denmark, 2012.

[40] Ö. Göksu, R. Teodorescu, C. L. Bak, F. Iov, and P. C. Kjær, "Instability of wind turbine converters during current injection to low voltage grid faults and PLL frequency based stability solution," *IEEE Trans. Power Syst.*, vol. 29, no. 4, pp. 1683−1691, Jul. 2014.

[41] D. Dong, B. Wen, D. Boroyevich, P. Mattavelli, and Y. Xue, "Analysis of phase-locked loop low-frequency stability in three-phase grid-connected power converters considering impedance interactions," *IEEE Trans. Ind. Electron.*, vol. 62, no. 1, pp. 310−321, Jan. 2015.

[42] H. Wu and X. Wang, "Design-oriented transient stability analysis of PLL-synchronized voltage-source converters," *IEEE Trans. Power Electron.*, in press, DOI: 10.1109/TPEL.2019.2937942.

[43] S. H. Strogatz, *Nonlinear Dynamics and Chaos: With Applications to Physics, Biology, Chemistry, and Engineering*, 2nd ed. Boca Raton, FL, USA: CRC Press, 2018.

[44] G. C. Goodwin, S. F. Graebe, and M. E. Salgado, *Control System Design*. Upper Saddle River, NJ, USA: Prentice-Hall, 2000.

[45] S. D'Arco, J. A. Suul, and O. B. Fosso, "A virtual synchronous machine implementation for distributed control of power converters in smart grids," *Electr. Power Syst. Res.*, vol. 122, pp. 180−197, May 2015.

[46] J. A. Suul, S. D'Arco, and G. Guidi, "Virtual synchronous machine-based control of a single-phase bi-directional battery charger for providing vehicle-to-grid services," *IEEE Trans. Ind. Appl.*, vol. 52, no. 4, pp. 3234−3244, Jul./Aug. 2016.

Donghua Pan (S'12-M'15) received the B.S. and Ph.D. degrees in electrical engineering from Huazhong University of Science and Technology, Wuhan, China, in 2010 and 2015, respectively.

Since September 2017, he has been with Aalborg University, Aalborg, Denmark, where he is currently a Postdoctoral Fellow with the Department of Energy Technology. His research interests include magnetic integration techniques, modeling and control of grid-connected converters, and wide bandgap power conversion systems.

Dr. Pan was the recipient of the Outstanding Reviewer Award of IEEE TRANSACTIONS ON POWER ELECTRONICS in 2017 and the Best Paper Award at IEEE SPEC 2018.

Xiongfei Wang (S'10-M'13-SM'17) received the B.S. degree from Yanshan University, Qinhuangdao, China, in 2006, the M.S. degree from Harbin Institute of Technology, Harbin, China, in 2008, both in electrical engineering, and the Ph.D. degree in energy technology from Aalborg University, Aalborg, Denmark, in 2013.

Since 2009, he has been with the Department of Energy Technology, Aalborg University, where he became Assistant Professor in 2014, Associate Professor in 2016, Professor and Research Program Leader for Electronic Power Grid (eGrid) in 2018. His current research interests include modeling and control of grid-interactive power converters, stability and power quality of power electronic based power systems, active and passive filters.

Dr. Wang was selected into Aalborg University Strategic Talent Management Program in 2016. He received six IEEE prize paper awards, the 2016 outstanding reviewer award of IEEE TRANSACTIONS ON POWER ELECTRONICS, the 2018 IEEE PELS Richard M. Bass Outstanding Young Power Electronics Engineer Award, the 2019 IEEE PELS Sustainable Energy Systems Technical Achievement Award, and the 2019 Highly Cited Researcher in the Web of Science. He serves as an Associate Editor for the IEEE TRANSACTIONS ON POWER ELECTRONICS, the IEEE TRANSACTIONS ON INDUSTRY APPLICATIONS, and the IEEE JOURNAL OF EMERGING AND SELECTED TOPICS IN POWER ELECTRONICS.

Fangcheng Liu received the B.S. degree from Huazhong University of Science and Technology, Wuhan, China, in 2007, the Ph.D. degree from Xi'an Jiaotong University, Xi'an, China, in 2014, both in electrical engineering. Since 2014, he has been with Huawei, where he is currently a Researcher of Watt Laboratory (Part of Central Research Institute). His main research interests include modeling and control of grid-connected converters and stability of power electronic based power systems.

Rongliang Shi (S'13) received the B.S. and Ph.D. degrees from Hefei University of Technology, Hefei, China, in 2011 and 2017, respectively, both in electrical engineering. Since 2017, he has been with Huawei Technologies Co., Ltd., Shanghai, China, as an R&D Engineer. His research interests include control of VSG converters, paralleled converter systems, and distributed generation technologies.